Journal of Nuclear Materials 555 (2021) 153136

Contents lists available at ScienceDirect

Journal of Nuclear Materials

journal homepage: www.elsevier.com/locate/jnucmat

Effect of He content on the evolution of He bubbles and He thermal desorption behaviors in FeCr based nanocrystalline film

Le Wang[a,b,c], Qunbo Fan[a,b,*], Xianping Wang[c], Jiahao Yao[a], Yu Zhou[a], Yi Peng[a], Hao Ma[b], Xinyu Shen[b], Banglei Zhao[c], Jiangang Ke[c]

[a] Beijing Institute of Technology Chongqing Innovation Center, Chongqing 401135, China
[b] National Key Laboratory of Science and Technology on Materials Under Shock and Impact, School of Materials Science and Engineering, Beijing Institute of Technology, Beijing 100081, China
[c] Key Laboratory of Materials Physics, Institute of Solid State Physics, HF IPS, Chinese Academy of Sciences, Hefei 230031, China

ARTICLE INFO

Article history:
Received 23 February 2021
Revised 5 May 2021
Accepted 6 June 2021
Available online 15 June 2021

Keywords:
FeCr
Helium bubbles
Evolution
Thermal desorption
Magnetron sputtering

ABSTRACT

He-charged FeCr based nanocrystalline films were fabricated at room temperature in a mixed atmosphere of He and Ar by radio frequency magnetron sputtering. The effect of the He/Ar ratio on the crystalline structure, surface morphology, He desorption behaviors, and the size and distribution of He bubbles had been investigated by X-ray diffraction (XRD), scanning electron microscopy (SEM), thermal desorption spectrum (TDS), and transmission electron microscopy (TEM), respectively. The results of XRD revealed that He-charged FeCr based films had a typical bcc structure. Surface SEM images showed that the grain size of FeCr based films decreased with the He/Ar ratio increasing. The results of TDS profiles exhibited that these desorption peaks corresponded to the release of He atoms dissociated from surface, He_nV ($2 \le n \le 6$), He_nV_m ($1 \le n$, $2 \le m$), and He bubbles, respectively. Based on the results of TEM observation, the density of He bubbles was proportional to the He/Ar ratio, while the size of He bubbles could be scarcely influenced by the He/Ar ratio.

1. Introduction

FeCr based steels have been recognized as one of the most important candidates of structural materials for fusion reactors and advanced fission reactors, due to their good thermal conductivity, low corrosion, and high resistance to irradiation-induced swelling [1–3]. Besides, He atoms are often produced through (n, α) reactions and ternary fission in fusion and fission reactors [4]. As is well known, He atoms are extremely low insoluble in metals and are mobile due to their low migration energy of 0.078eV in steels [5]. Therefore, He atoms trapped by the defects can easily migrate, diffuse, and accumulate in steels. These accumulated He atoms can be trapped easily by radiation-induced defects, which has a strong tendency to promote He bubbles nucleation and growth. The presence of He bubbles can result in performance degradation of the structural materials, such as fast creep rupture, swelling, and embrittlement [6, 7].

Nanostructured materials have been exhibited to have excellent resistance to irradiation due to the high dislocation density and the large volume fraction of grain boundaries which can act as an important sink for radiation-reduced defects [8–11]. Many experimental studies about some radiation effects especially He effects on nanocrystalline materials have also been reported [12–15]. However, for He effects on nanocrystalline FeCr-based alloy, they were still rarely studied yet. Therefore, a detailed study about He effects on the properties of nanocrystalline FeCr-based alloy is very necessary, which can be helpful for the improvement of FeCr based alloy as the nuclear structural material.

There are many methods to introduce He atoms into samples, including ion implantation [16–18], radioactive decay of tritium [19–22] and neutron irradiation [23–27]. For the above ways, they still have some disadvantages in the process of He atom introduction. For example, He ion implantation can introduce controlled and quantitative He atoms into the investigated samples, but it is difficult to make these introduced He atoms distribute uniformly in materials. Also, for the radioactive decay of tritium, although it can introduce homogeneously He atoms into materials, the experiment process requires a long half-life radioactive period (about 12.3 years). Furthermore, neutron irradiation can cause a serious of irradiation-induced damage, which makes the study of He behavior more complex.

In recent years, an effective and convenient way of magnetron sputtering in He/Ar mixed atmosphere is developed to obtain

* Corresponding author.
E-mail address: fanqunbo@bit.edu.cn (Q. Fan).

https://doi.org/10.1016/j.jnucmat.2021.153136
0022-3115/

He-charged metal nanocrystalline. This technique was initially reported by Mattox and Kominiak [28] to capture He atoms into Au films. Nowadays, it has been developed to prepare other He-charged metal films, such as He-charged Al films [29], Cu films [30], Ti films [31] and W films [32–34] and so on. What's more, some experimental results have also demonstrated that different He concentrations can be achieved by adjusting the ratio of He/Ar fluxes to the vacuum chamber [29, 33].

In the present work, He-charged FeCr based nanocrystalline films were fabricated by radio frequency (RF) magnetron sputtering in a gas mixture of He and Ar. X-ray diffraction (XRD) and scanning electron microscopy (SEM) were used to characterize the crystalline structure and microstructure of FeCr based films with various He content. The element energy dispersive X-ray spectrometer (EDS) was used to confirm the element composition of samples. The desorption behaviors of He in FeCr based films were studied using thermal desorption spectroscopy (TDS). Besides, the amount, size and distribution of He bubbles were investigated by transmission electron microscopy (TEM).

2. Experimental

FeCr based films with He and without He were prepared by RF magnetron sputtering. A FeCr based alloy (Fe18Cr alloy) block (60 mm in diameter and 3 mm in thickness) was used as the sputtering target. The distance between the target and the substrate was 5 cm. The magnetron sputtering cavity before sputtering was pumped to a base pressure below 8.0×1.0^{-4} Pa by a turbomolecular pump. The work gases were Ar gas and He gas. The target was water-cooled so that the temperature could be kept at 20°C during the sputtering process. The FeCr based films were deposited onto Si (111) single crystal sheets (10.0 mm × 10.0 mm × 0.5 mm) at room temperature. Prior to the deposition, the Si substrates were firstly cleaned with a 3% HF solution etching to remove any SiO_2 from the surface, then washed out by deionized (DI) water in an ultrasonic washer for several minutes. All FeCr based films were deposited for 4 h at the work gas pressure of 1.0 Pa and deposited power of 70 W. To acquire FeCr films containing different He contents, the He/Ar ratio was adjusted at 0, 1:1, 2:1 and 4:1, respectively.

The crystal structure of FeCr films prepared under different He/Ar ratios was investigated by XRD (A Philips X'pert PRO) at a small incident angle of 1° with Cu-Kα radiation (wavelength: 0.15418nm). XRD patterns in the 2θ range were recorded from 30° to 90° with a step size of 0.02°. The surface and cross-section morphology of the deposited films was confirmed by field emission scanning electron microscopy (FESEM, Sirion 200 FEG). The secondary electrons produced by a 5 keV electron beam were detected by the in-lens detectors system. The element composition of the deposited films was evaluated by an energy dispersive X-ray spectrometer (EDS) analysis using EDX XFlash 3001 detector and the Oxford Instruments INCA Energy system. The accelerating voltage used was 10 keV. Helium release characteristics in FeCr films were measured by thermal desorption spectroscopy (TDS). The film samples were linearly heated up to 1000°C after about 100 min (10°C/min) and then remained for 30 min. He released from samples was detected with a quadruple mass spectrometer (QMS). Through collecting the mass spec response of He versus sample temperature, He desorption behaviors can be obtained and analyzed. The size and amount of He bubbles were confirmed by TEM (JEOL-2100, Japan) with an accelerating voltage of 200 kV. The film TEM samples were made using a complex method. First, we cut film samples deposited on Si substrates into two same rectangular slices (3 mm × 2 mm × 0.5mm). The two slices were glued face to face using a Gatan G1 epoxy glue to make a sandwich consisting of the Si/films/glue/films/Si layers. Then the sandwich was held in a copper ring with 3 mm outer diameter and 2 mm inner diameter. The samples were thinned by mechanical polishing on abrasive paper of P3000 until to obtain a thickness lower than 10 μm and then argon ion milling on both sides (ion beam angles equal to $+4^\circ$ and -4°). In order to estimate the number density of He bubbles, the local thickness of TEM samples was measured by EELS log-ratio approach, which causes an uncertainty of ±10% [35]. The thickness of the observed region of TEM specimen is ~80 nm in this work.

3. Results and discussion

3.1. Crystalline structure and microstructure of FeCr films

XRD patterns of FeCr films prepared under different He/Ar ratios are shown in Fig. 1(a). Two diffraction peaks are observed in the XRD patterns, which can be assigned as the (110) and (211) planes of Fe phase. As shown in Fig. 1(a), with the increase of He/Ar ratio, the diffraction patterns show a remarkable line broadening trend. It indicates that the line broadening should be the cause of the trapped He atoms during the film deposition process. A similar phenomenon was also reported by Shi [31] and Jia [29]. In their work, they claimed that the broadening of the diffraction peaks should be the results of the lattice distortion and grain refinement. Furthermore, the lattice distortion can also lead to the shift of peak position. However, in our work, the peak position was not shifted in the XRD patterns. Moreover, dislocation can also cause the peak broadening [36, 37]. Also, although the dislocations were found in deposited FeCr films in the subsequent experiments, the dislocation density was very low. This suggest that the effects of the dislocation and the stress on the peak broadening can be negligible, and the diffraction peak broaden should be mainly caused by grain size. Despite we cannot calculate the accurate grain size by the results of XRD patterns due to the limitation of the XRD method, the decreasing trend of the grain size with the He/Ar ratio increasing should be convincing. That is, the addition of He during film deposition can cause the refinement of grain.

Fig. 2(a-d) show the surface morphologies of FeCr films deposited under different He/Ar ratios at RT. As shown in Fig. 2(a-d), all the FeCr films exhibit a completely dense microstructure, in which many spherical grains are observed. The addition of He induced the change of surface morphology of FeCr films. With He content increasing, the grain size was reduced. In a word, He atoms, which was introduced into FeCr films, can refine the grains

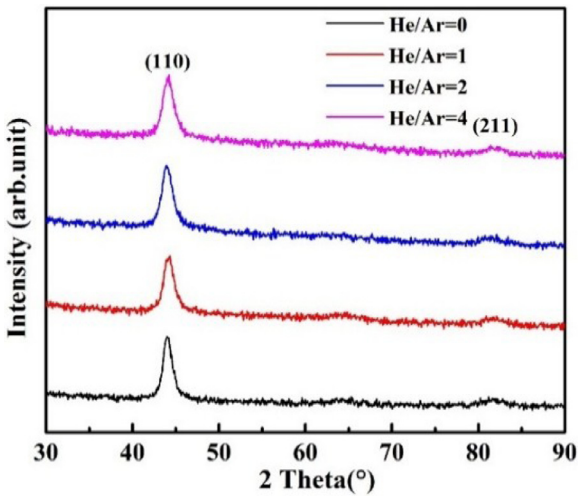

Fig. 1. (a) XRD patterns of FeCr films fabricated on Si substrates at RT under different He/Ar ratios of 0, 1:1, 2:1, and 4:1.

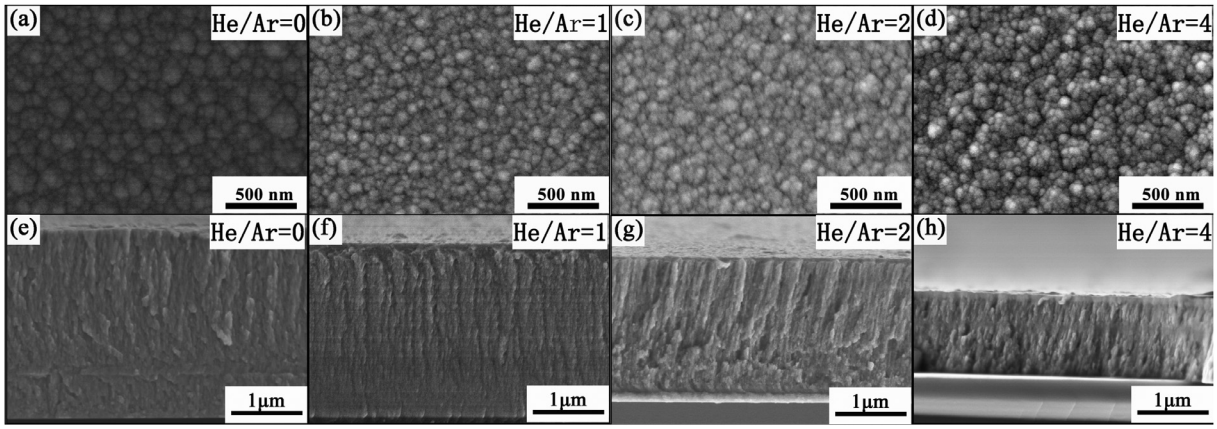

Fig. 2. Surface and cross-sectional morphology and of FeCr based films deposited on Si substrates at RT under various He/Ar ratios: (a) and (e) 0; (b) and (f) 1:1; (c) and (g) 2:1; (d) and (h) 4:1.

Table 1
Element composition of FeCr based films fabricated under varying He/Ar ratios.

He/Ar ratio	Cr (wt.%)	Fe (wt.%)
0	16±0.2	84±0.2
1	15±0.3	85±0.3
2	17±0.1	83±0.1
4	16±0.2	84±0.3

of these films and improve the roundness and uniformity of globular grains. The cross-section morphologies of FeCr films were presented in Fig. 2(e-h). These films have the typical columnar crystal structure. The film thickness ranges from 1.2 μm to 2.8 μm. The differences in grain sizes of these films were not easy to be distinguished from the cross-section morphologies of films, because the grain sizes are very small and the columnar crystal structures are very dense.

Table 1 shows that the results of EDS analysis for FeCr based films synthesized under different He/Ar ratios. As presented in Table 1, each film contains the nearly same amount of Fe and Cr. This indicates that the effects of the He/Ar ratio in the mixed gas on the element composition of the deposited films can be ignored. It is worth noting that He can't be detected by EDS because EDS isn't sensitive to light elements, especially H and He.

3.2. He desorption behaviors of FeCr based films containing helium

The TDS profiles of FeCr films fabricated on Si substrates under different He/Ar ratios (0, 1:1, 2:1, 4:1) at RT are shown in Fig. 3. As presented in Fig. 3, the integrated intensity of desorption peaks increases with the He/Ar ratio increasing, which is consistent with the positive correlation between the He concentration and the He/Ar ratio of the mixed gas. It is obvious that there is no He releasing peak in the films at He/Ar=0 due to no He atoms. For the FeCr films prepared at He/Ar=1, 2 and 4, the released signal can be divided into four groups. In general, Group I is located at 250°C~400°C, the second desorption peaks (Group II) occur around 600°C, Group III is shifted to a temperature range (800°C-850°C) and Group IV is obtained at the higher temperature (>1000°C).

From the results of TDS profiles shown in Fig. 3, the activation energies corresponding to the various He desorption peaks can be calculated. In general, based on simple first-order dissociation kinetics, the desorption process is described by the followed equation [38, 39]:

$$\frac{dn}{dt} = -\nu N \exp(-E/(k_B T)) \quad (2)$$

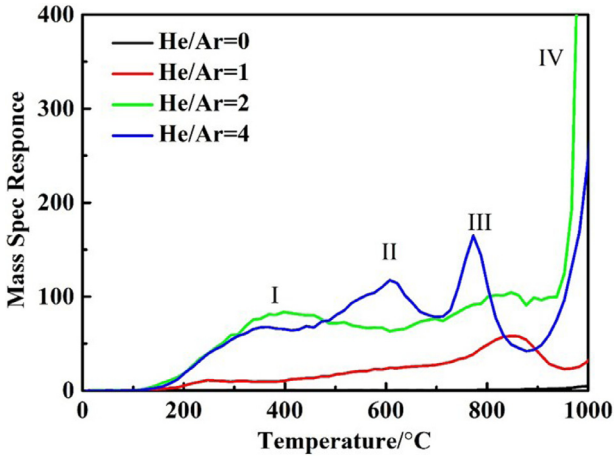

Fig. 3. Thermal desorption spectrum of FeCr films deposited on Si substrates at RT under different He/Ar ratios of 0, 1:1, 2:1 and 4:1, respectively.

Table 2
Desorption temperature and desorption energy.

Desorption temperature (K)	Desorption energy (eV)
673	1.9
873	2.5
1073	3.07

Where N is the number of defects trapping He atoms at temperature T. ν is the jumping frequency (assumed to be 10^{13}/s), E is the He desorption activation energy for the specific capture site. k_B is the Boltzman constant.

In this study, the heating process was carried out at a constant heating rate, the peak temperature T_p and the desorption energy E obey the following equation [40, 41]:

$$2lnT_p - ln\beta = E/k_B T_p + ln(E/(k_B T)) \quad (3)$$

According to the Redhead equation [42], the He desorption energy E is reckoned as:

$$E = (ln(\nu T_p/\beta) - 3.64)k_B T_p \quad (4)$$

The desorption energy of He atoms from the various defects was estimated by the above Eq. (4). The results of desorption energy for the specific desorption temperature are shown in Table 2.

When He/Ar=1 and 2, the profiles didn't present in Group II. However, the profile arose the Group II located at 600°C. In the case of He-charged FeCr films, Group I mainly is attributed to the

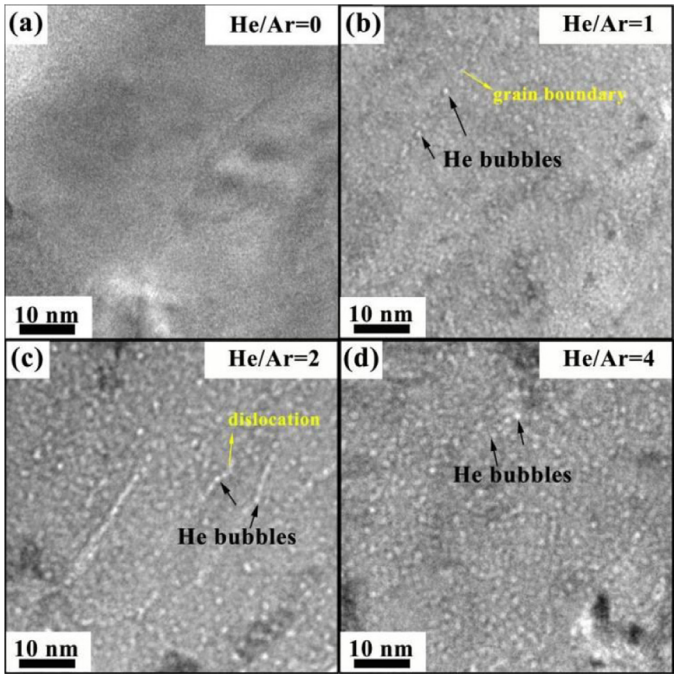

Fig. 4. TEM images of FeCr films prepared at RT under different He/Ar ratios of (a) 0, (b) 1:1, (c) 2:1, and (d) 4:1, respectively.

release of He trapped by a vacancy in the neighborhood of the surface, these He atoms are trapped during the deposition process and are dissociated during the low-temperature annealing [43]. The temperature of Group II and Group III is close to that of the desorption of He from in He_nV ($2 \leq n \leq 6$) and He_nV_m ($1 \leq n$, $2 \leq m$) [44–47]. For Group III, the desorption temperature is about 850°C when He/Ar=1 and 2. While the desorption temperature is 780°C when He/Ar=3. This means that the He atoms can be easily dissociated from He_nV_m easily when the He/Ar ratio increase. This is because the binding energy of He atoms to the He_nV_m cluster decreases as the He-to-vacancy ratio increase [48]. Therefore, the increased He/Ar ratios can result in a higher He-to-vacancy ratio in the deposited films, which may make He atoms release at the lower temperature. There is no He desorption peaks (850°C-950°C) due to γ-transformation in FeCr films. The result is similar to that of Fe-Cr alloys implanted by He^+ ion [49]. For Group IV (>1000°C), it may be ascribed to the release of He atoms from bubbles. The above results demonstrated that different types of He atoms can be introduced into the deposited FeCr films. Meanwhile, from the TDS spectra, more He atoms were implanted into the FeCr films with the increasing He/Ar ratio, which was consistent with the results of the following TEM observation.

3.3. Size and distribution of He bubbles

TEM observations with an under-focus condition (~800 nm) were performed in Fig. 4 to characterize the morphology and distribution of He bubbles. Fig. 4(a) shows that a large number of bubbles are homogeneously dispersed in the deposited films. This phenomenon is consistent with the result of O. El-Atwani et al. [50] in which they found that He bubbles were distributed uniformly in UFG and NC tungsten bombarded with 8keV He^+ ion at RT during an in-situ experiment. Similar results were also reported by P. D. Edmondson et.al. [51]. In their study, it was relatively uniform that the size distribution of He bubbles measured from the regions of the highest slope of concentration for the samples irradiated to 6.75×10^{20} He m^{-2}. However, a significantly inhomogeneous size distribution was observed in the TEM images of the

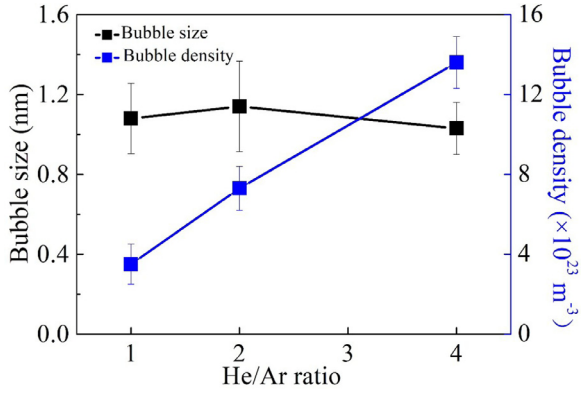

Fig. 5. Diameter size and density of He bubbles in FeCr films prepared at RT under different He/Ar ratios of 1:1, 2:1 and 4:1, respectively.

samples irradiated to 2.25×10^{21} He m^{-2}. This is because that the high dose He^+ ions may induce some bubble agglomeration [52]. Therefore, the distribution of He bubbles introduced by magnetron sputtering is similar to the result acquired by a low dose of He^+ ion implantation.

As shown in Fig. 4(a) and (b), grain boundaries and dislocations are decorated by He bubbles. The preferential nucleation sites for He bubbles may be attributed to misfit dislocation, grain boundary orientation and free volume regions at the grain boundaries [52, 12]. Specifically, vacancies were produced during magnetron sputtering which could easily accumulation at grain GBs. These vacancies trapped by GBs may drag He atoms to GBs as a result of the He-vacancy affinity. Generally, the migration energy of He in the metal lattice is very small, and the binding energy of He to vacancies along GBs is strong. Thus, the introduced He atoms would easily diffuse to precipitation into He-vacancy clusters and then grow into bubbles. Besides, to obtain the effect of He/Ar ratio on He bubble size, 300 He bubble diameters were measured in TEM images. As shown in Fig. 5, when He/Ar=1, He bubble diameter is about 0.9 nm. When He/Ar=2, He bubble diameter is 1.1 nm, and when He/Ar=4, the diameter of bubbles is about 1 nm. This indicates that He bubble diameter has no significant change with the He/Ar ratios increasing. It can be seen that the bubble density increased when the He/Ar ratio increased. This is because with the increase of He/Ar ratio, more He atoms can be trapped into the deposited FeCr films, which can contribute to forming more He bubbles. The result is also identical to the TDS profile shown in Fig. 3. What's more, utilizing the detailed calculations, the bubble density was found to be proportion to the He/Ar ratio. However, the positive relationship between the bubble density and He/Ar ratio is only an approximation. In the actual deposition process, with the increase of the He/Ar ratio, the probability of collision among He atoms and He atoms each other may also increase, which will result in the density of the implanted He atoms less than that in the ideal case. The above results suggested that He bubbles with a specific number density could be introduced into the investigated samples by magnetron sputtering, which will be a benefit for the future study of nuclear materials, particularly the study of He effects on nuclear structural materials.

4. Conclusion

FeCr films with various He concentrations were prepared in the mixed atmospheres with different He/Ar ratios. XRD and EDS analysis exhibited the evolution of the structure and main element compositions of He-charged FeCr films. SEM observations and XRD analysis suggested that the grain size of films decreased with the He/Ar ratio increasing. The results of TDS showed that He-charged

FeCr based films fabricated under different He/Ar ratios (0, 1:1, 2:1, 4:1) at RT had different desorption peaks. These peaks could be divided into four groups: Group I (250°C-400°C), Group II (around 600°C), Group III (850°C-950°C) and Group IV (above 900°C), which were assigned to the release of He atoms dissociated from surface, He_nV_m complexes, and He bubbles, respectively. Meanwhile, the position of the corresponding desorption peaks was shifted to the lower temperature when the He/Ar ratio increased due to the increase of the He-to-vacancy ratio**.** TEM images suggested that He bubbles were distributed homogeneously in the grain interiors, and the size of He bubbles had no noticeable change with the increase of the He/Ar ratio.

Data availability

The raw/processed data required to reproduce these findings cannot be shared at this time due to legal or ethical reasons.

Declaration of Competing Interest

The authors declare that they have no known competing financial interests or personal relationships that could have appeared to influence the work reported in this paper.

CRediT authorship contribution statement

Le Wang: Conceptualization, Methodology, Writing – original draft, Funding acquisition. **Qunbo Fan:** Methodology, Visualization, Funding acquisition. **Xianping Wang:** Methodology, Resources. **Jiahao Yao:** Methodology, Resources. **Yu Zhou:** Supervision, Writing – review & editing. **Yi Peng:** Supervision, Writing – review & editing. **Hao Ma:** Investigation. **Xinyu Shen:** Investigation. **Banglei Zhao:** Investigation. **Jiangang Ke:** Investigation.

Acknowledgment

This work was financially supported by the Chongqing Nature Science Foundation (Grant Nos.: cstc2020jcyj-msxmX0094), Project funded by China Postdoctoral Science Foundation (Grant Nos.: 2020M680372) and Project funded by Chongqing Postdoctoral Science Foundation (Grant Nos.: 2021ZX5200007).

References

[1] E.E. Bloom, S.J. Zinkle, F.W. Wiffen, Materials to deliver the promise of fusion power-progress and challenges, J. Nucl. Mater. 329-333 (2004) 12–19.
[2] J.L. Boutard, The structural materials for the first wall and plasma facing components of NET, J. Nucl. Mater. 174 (1990) 240–252.
[3] S. Şahin, M. Übeyli, A review on the potential use of austenitic stainless steels in nuclear fusion reactors, J. Fusion Energ. 27 (2008) 271–277.
[4] J. Van den Bosch, G. Coen, R.W. Bosch, A. Almazouzi, TWIN ASTIR: First tensile results of T91 and 316L steel after neutron irradiation in contact with liquid lead-bismuth eutectic, J. Nucl. Mater. 398 (2010) 68–72.
[5] R. Kemp, G. Cottrell, H.K.D Bhadeshia, Classical thermodynamic approach to void nucleation in irradiated materials, Energy Mater. 1 (2) (2006) 103–105.
[6] H.T. Weaver, W.J. Camp, Detrapping of interstitial helium in metal tritides-NMR studies, Phys. Rev. B. 12 (1975) 3054.
[7] R. Schäublin, J. Henry, Y. Dai, Helium and point defect accumulation:(i) microstructure and mechanical behaviour, C. R. Phys. 9 (3-4) (2008) 389–400.
[8] A.R. Kilmamentov, D.V. Gunderov, R.Z. Valiev, A.G. Balogh, H. Hahn, Enhanced ion irradiation resistance of bulk nanocrystalline TiNi alloy, Scr. Mater. 59 (2008) 1027–1030.
[9] N. Nita, R. Schaeublin, M. Victoria, Impact of irradiation on the microstructure of nanocrystalline materials, J. Nucl. Mater. 329-333 (2004) 953–957.
[10] H. Gleiter, Nanocrystalline materials, Prog. Mater. Sci. 33 (1989) 223–315.
[11] S. Wurstera, R. Pippan, Nanostructured metals under irradiation, Scr. Mater. 60 (2009) 1083–1087.
[12] P.D. Edmondson, C.M. Parish, Y. Zhang, A. Hallén, M.K. Miller, Helium entrapment in a nanostructured ferritic alloy, Scr. Mater. 65 (2011) 731–734.
[13] T. Yamamoto, Y. Wu, G.R. Odette, K. Yabuuchi, S. Kondo, A. Kimura, A dual ion irradiation study of helium-dpa interactions on cavity evolution in tempered martensitic steels and nanostructured ferritic alloys, J. Nucl. Mater. 449 (2014) 190–199.
[14] Q. Li, C.M. Parish, K.A. Powers, M.K. Miller, Helium solubility and bubble formation in a nanostructured ferritic alloy, J. Nucl. Mater. 445 (2014) 165–174.
[15] K.Y. Yu, Y. Liu, C. Sun, H. Wang, L. Shao, E.G. Fu, X. Zhang, Radiation damage in helium ion irradiated nanocrystalline Fe, J. Nucl. Mater. 425 (2012) 140–146.
[16] M. Tokitani, M. Miyamoto, K. Tokunaga, H. Iwakiri, T. Fujiwara, N. Yoshida, Desorption of helium from austenitic stainless steel heavily bombarded by low energy He ions, J. Nucl. Mater. 329-333 (2004) 761–765.
[17] Y. Hidaka, S. Ohnuki, H. Takahashi, S. Watanabe, Effect of He on void formation and radiation-induced segregation in dual-beam irradiated Fe-Cr-Ni, J. Nucl. Mater. 212-215 (1994) 330–335.
[18] S.M. Myers, W.R. Wampler, Effect of He on void formation and radiation-induced segregation in dual-beam irradiated Fe-Cr-Ni, J. Nucl. Mater. 111-112 (1982) 579–583.
[19] J.R. Cost, R.G. Hickman, Helium release from various metals, J. Vat. Sci. Tech. 12 (1975) 516.
[20] S.L. Robinson, N.R. Moody, The effect of hydrogen, tritium and decay helium on the fracture toughness of a stainless steel superalloy, J. Nucl. Mater. 140 (1986) 245–251.
[21] A.M. Brass, A. Chanfreau, J. Chene, Helium 3 precipitation in AISI 316L stainless steel induced by radioactive decay of tritium: microstructural study of helium bubble precipitation, Metal. Mater. Trans. 25 (1994) 2117–2130.
[22] G.R. Caskey Jr., D.E. Raw1 Jr., D.A. Mezzanote Jr., Helium embrittlement of stainless steels at ambient temperature, Scr. Met. 16 (1982) 969–972.
[23] H.J. Jung, D.J. Edwards, R.J. Kurtz, T. Yamamoto, Y. Wu, G.R. Odette, Structural and chemical evolution in neutron irradiated and helium-injected ferritic ODS PM2000 alloy, J. Nucl. Mater. 484 (2017) 68–80.
[24] S.J. Zinkle, P.J. Maziasz, R.E. Stoller, Dose dependence of the microstructural evolution in neutron-irradiated austenitic stainless steel, J. Nucl. Mater. 206 (1993) 266–286.
[25] A. Alsabbagh, A. Sarkar, B. Miller, J. Burns, L. Squires, D. Porter, J.I. Cole, K.L. Murty, Microstructure and mechanical behavior of neutron irradiated ultrafine grained ferritic steel, Mater. Sci. Eng. A 615 (2014) 128–138.
[26] K.G. Fields, X. Hu, K.C. Littrell, Y. Yamamoto, L.L. Snead, Radiation tolerance of neutron-irradiated model Fe-Cr-Al alloys, J. Nucl. Mater. 465 (2015) 745–755.
[27] P.D. Edmondson, S.A. Briggs, Y. Yamamoto, R.H. Howard, K. Sridharan, K.A. Terrani, K.G. Field, Irradiation-enhanced α' precipitation in model FeCrAl alloys, Scr. Mater. 116 (2016) 112–116.
[28] D.M. Mattox, G.J. Kominiak, Incorpation of helium in deposited gold films, J. Vac. Sci. Technol. 8 (1971) 194.
[29] J.P. Jia, L.Q. Shi, X.C. Lai, Q.F. Wang, Preparation of Al thin films charged with helium by DC magnetron sputtering, Nucl. Instrum. Methods Phys. Res., Sect. B 263 (2007) 446–450.
[30] Q. Qi, X.F. Wang, L.Q. Shi, L. Zhang, B. Zhang, Y.F. Lu, A. Liu, Investigation on thermal release behavior of helium-charged copper films by DC magnetron sputtering fusion, Sci. Technol. 60 (2011) 1483–1486.
[31] L.Q. Shi, C.Z. Liu, S.L. Xu, Z.Y. Zhou, Helium-charged titanium films deposited by direct current magnetron sputtering, Thin Solid Films 479 (2005) 52–58.
[32] L. Wang, T. Hao, B.L. Zhao, T. Zhang, Q.F. Fang, C.S. Liu, X.P. Wang, L. Cao, Evolution behavior of helium bubbles and thermal desorption study in helium-charged tungsten film, J. Nucl. Mater. 508 (2018) 107–115.
[33] L. Wang, Q.B. Fan, T. Hao, D.duo Wang, X.J. Zhu, H.C. Gong, X. Liu, Effect of He content on microstructure, mechanical properties and He thermal desorption behavior of W film fabricated by RF magnetron sputtering, J. Nucl. Mater. 534 (2020) 152151.
[34] L. Wang, T. Hao, B.L. Zhao, R. Liu, Q.F. Fang, C.S. Liu, X.P. Wang, L. Cao, J.L. Chen, The effect of Y_2O_3 addition on He desorption behavior and He bubble evolution in He-charged W-Y_2O_3 film, Thin Solid Films 709 (2020) 138184.
[35] T. Malis, S.C. Cheng, R.F. Egerton, EELS log-ratio technique for specimen thickness measurement in the TEM, J. Electron Microsc. Tech. 8 (1988) 193–200.
[36] TUngár, Microstructural parameters from X-ray diffraction peak broadening, Scr. Mater. 51 (8) (2004) 777–781.
[37] N. Sallez, X. Boulnat A. Borbély, J.L. Béchade, D. Fabrègue, M. Perez, Y.de D. Carlan, L. Hennet, C. Mocuta, D. Thiaudière, Y. Bréchet, In situ characterization of microstructural instabilities: recovery, recrystallization and abnormal growth in nanoreinforced steel powder, Acta Mater. 87 (2015) 377–389.
[38] Y.H. Gong, X.Z. Cao, S.X. Jin, E.Y. Lu, Y.C. Hu, T. Zhu, P. Kuang, Q. Xu, B.Y. Wang, Effect of dislocations on helium retention in deformed pure iron, J. Nucl. Mater. 482 (2016) 93–98.
[39] T. Zhu, X.Z. Cao, S.X. Jin, J.P. Wu, Y.H. Gong, E.Y. Lu, B.Y. Wang, R.S. Yu, L. Wei, Helium retention and thermal desorption from defects in Fe9Cr binary alloys, J. Nucl. Mater. 466 (2015) 522–525.
[40] B. Janković, B. Adnađević, S. Mentus, The kinetic study of temperature-programmed reduction of nickel oxide in hydrogen atmosphere, Chem. Eng. Sci. 63 (2008) 567–575.
[41] M. Yajima, N. Yoshida, S. Kajita, M. Tokitani, T. Baba, N. Ohnoa, In situ observation of structural change of nanostructured tungsten during annealing, J. Nucl. Mater. 449 (1-3) (2014) 9–14.
[42] P.A. Redhead, Thermal desorption of gases, Vacuum 12 (1962) 203–211.
[43] R. Sugano, K. Morishita, A. Kimura, H. Iwakiri, N. Yoshida, Microstructural evolution in Fe and Fe-Cr model alloys after He^+ ion irradiations, J. Nucl. Mater. 329-333 (2004) 942–946.
[44] K. Ono, K. Arakawa, H. Shibasaki, H. Kurata, I. Nakamichi, N. Yoshida, Release of helium from irradiation damage in Fe-9Cr ferritic alloy, J. Nucl. Mater. 329-333 (2004) 933–937.

[45] R. Sugano, K. Morishita, H. Iwakiri, N. Yoshida, Effects of dislocation on thermal helium desorption from iron and ferritic steel, J. Nucl. Mater. 307-311 (2002) 941–945.
[46] D. Xu, B.D. Wirth, Post-implantation thermal desorption of helium from poly- and single-crystalline iron, J. Nucl. Mater. 386-388 (2009) 395–399.
[47] K. Morishita, R. Sugano, H. Iwakiri, N. Yoshida, A. Kimura, Thermal helium desorption from α-iron, PRICM 4 (2001) 1395–1398.
[48] K. Morishita, R. Sugano, B.D. Wirth, T. Diaz de la Rubia, Thermal stability of helium-vacancy clusters in iron, Nucl. Instrum. Methods Phys. Res. Sect. B Beam Interact. Mater. Atoms. 202 (2003) 76–81.
[49] R. Sugano, K. Morishita, A. Kimura, Helium accumulation behavior in iron based model alloys, Fus. Sci. Technol. 44 (2003) 446–449.
[50] O. El-Atwani, K. Hattar, J.A. Hinks, G. Greaves, S.S. Harilal, A. Hassanein, Helium bubble formation in ultrafine and nanocrystalline tungsten under different extreme conditions, J. Nucl. Mater. 458 (2015) 216–223.
[51] P.D. Edmondson, C.M. Parish, Y. Zhang, A. Hallén, M.K. Miller, Helium bubble distributions in a nanostructured ferritic alloy, J. Nucl. Mater. 434 (1-3) (2013) 210–216.
[52] P.L. Lane, P.J. Goodhew, Helium bubble nucleation at grain boundaries, Philos. Mag. A. 48 (1983) 965–986.